Journal of Civil Structural Health Monitoring (2024) 14:1075–1090
https://doi.org/10.1007/s13349-024-00774-0

ORIGINAL PAPER

Dynamic monitoring of a masonry arch rail bridge using a distributed fiber optic sensing system

Liangliang Cheng[1] · Alfredo Cigada[2] · Emanuele Zappa[2] · Matthew Gilbert[3] · Zi-Qiang Lang[4]

Received: 15 May 2022 / Accepted: 20 January 2024 / Published online: 1 March 2024

Abstract
Masonry arch bridges are an integral part of the European transportation infrastructure. Regular inspections are critical to ensure the safe operation of these bridges and also to preserve historical heritage. Despite recent advancements in assessment techniques, monitoring masonry arch bridges remains a difficult and important research topic. This paper describes a proof-of-concept study carried out on a masonry arch rail bridge in Gavirate, Italy, to investigate the dynamic responses of the bridge to train-induced moving loads. The dynamic measurements are obtained by a distributed fiber optic sensing system that enables a novel inspection of the integrity of masonry arch bridges. The focus of this field study is to quantify the dynamic strain induced by train moving loads and reveal the masonry arch bridge's dynamic behaviors through the use of an innovative distributed fiber optical sensing-based technique. The results may provide a useful guideline for the application of distributed fiber optical sensing to monitoring masonry arch bridges.

Keywords Masonry railway bridge · Distributed fiber optics · Strain measurement · Dynamic measurement · Structural health monitoring

1 Introduction

Masonry arch bridges comprise a significant portion of the railway bridge assets. They are the oldest structure types within the railroad bridge group, with thousands of bridges still in service, bearing the primary responsibility for Europe's transportation networks. Currently, modern transportation is heavily reliant on railway bridges, which are critical for transporting passengers and cargos, as well as driving regional and national economic growth.

According to Orbán's survey on masonry arch bridges [1], the railways participating in a project organized by the International Union of Railways (UIC) have over 200,000 masonry arch bridges and culverts along their route in Europe, accounting for approximately 60% of their total bridge stock. Additionally, it has been noted that the majority of masonry arch bridges (approximately 82%) are over 100 years old. And the state of preservation of masonry arch bridges varies from good to poor, with a proclivity for deterioration and even damage. Thus, assessment and maintenance of railway bridges are critical as they enable timely intervention to avoid serious damage or complete collapse.

Unlike conventional destructive testing, which is primarily concerned with the mechanical properties of materials, a variety of available Non-Destructive Testing (NDT) techniques, such as ultrasound, laser scanning, and ground-penetrating radar, are increasingly being used to obtain more confident assessments of masonry arch bridges [2–7].

In fact, railway bridges are subjected to significant impacts when loaded at high speeds, and the dynamic behaviors of these bridges are gaining attention and frequently serve as the determining factor in structural design [8]. As bridge damage is frequently interpreted as a loss of mechanical properties, such as stiffness, the modal parameters reflect this. As a result, by monitoring changes in dynamic properties, it is possible to determine whether or not a bridge structure has changed.

✉ Liangliang Cheng
liangliang.cheng@rug.nl

[1] ENTEG, Faculty of Science and Engineering, University of Groningen, Groningen, The Netherlands

[2] Department of Mechanical Engineering, Politecnico di Milano, Milan, Italy

[3] Department of Civil and Structural Engineering, The University of Sheffield, Sheffield, UK

[4] Department of Automatic Control and System Engineering, The University of Sheffield, Sheffield, UK

While these techniques instill confidence in the assessment results regarding the asset's current state, they are incapable of capturing the structure's dynamic response and revealing the structural degradation process. Attempts have been made to resolve these problems, including the use of accelerometers [9, 10], Digital Image Correlation (DIC) technologies [11–13], and Fiber Bragg Grating (FBG) sensors [14–16], among others. To name a few, the DIC technique has been used to quantify strain and localize cracks in small-scale masonry specimens in the laboratory, and a pilot test on a four-span railway masonry bridge in the field is presented in [13]. In [16], the FBG system is used to investigate into detailed typical dynamic structural responses of a skewed masonry arch railway bridge (North Yorkshire, UK) and to quantify its sensitivity to a variety of factors. Recent advances in the Distributed Fiber Optic Sensing (DFOS) technique [17–19] enable a dense measurement of physical quantities, such as strain and temperature, using a single fiber optic cable equipped with thousands of "strain gages" that can be flexibly attached to complex geometries. The authors have investigated the DFOS technique for experimental strain modal analysis [20] and a novel sensor fusion approach for the improvement of the measurement quality of distributed fiber optic sensors used in static and dynamic strain measurements [21, 22]. Regrettably, only a few applications of DFOS systems for monitoring masonry arch bridges have been reported in the up-to-date literature [16].

The standpoint of this paper is to present the results of a campaign test on a masonry arch rail bridge in Gavirate, Italy, using the Luna ODiSI-B® system [23], a DFOS with a high spatial resolution based on Optical Frequency Domain Reflectometry (OFDR), with the goal of determining the feasibility of DFOS-based monitoring and providing an initial understanding of the dynamic response under the loads produced by moving trains. By observing the strain distributions created by the moving loads, high-risk regions where potential damage could take place have been identified.

The objectives of the current investigation are fourfold:

(1) Installation of the fibers and configuration of the sensor placement, discussing potentially critical practical issues; (2) Application of distributed fiber optic sensing system (LUNA ODSIB system) to perform on-site monitoring and an evaluation of the obtained signal quality; (3) Determination and quantification of the full-field dynamic strain profile of the investigated span under train-induced moving loads; (4) Evaluation of the feasibility to assess the structural integrity of the monitored infrastructure such as the anomaly of strain sensing point that may correspond to the occurrence of local cracks.

The paper is structured as follows: the monitored masonry arch rail bridge is described in Sect. 2, followed by a detailed on-site monitoring set-up description in Sect. 3. Section 4 illustrates the data processing and measurement processes that have been used to reveal the bridge's dynamic behaviors. Section 5 provides a summary of the study and discusses possible future works.

2 The monitored structure

The monitored masonry arch rail bridge is located in the municipality of Gavirate at the progressive km. 40 of the Milano–Laveno railway line, which is a single-track line. It consists of six low arches with a span of 5 m and the seventh one with a slightly longer span of 6 m; all arches are assembled with a constant thickness equal to 68–70 cm. In cross section, the width of the roadway where the track is laid is equal to 4.20 m; On the Laveno side (the north side), there is a containment wall of the embankment about 61 m long.

The piles are 1.2 m thick and vary in height from the foundation clearance to the arch level between 2.5 and 3 m. The front walls are constructed of strong stone ashlars (probably coming from the Moltrasio quarries). In the end, there is a square stone crowning.

Figure 1a sows the bridge from the southwest, with Span 2, denoted by the red square, being the section examined in this paper (b). Figure 2 is a top view of the bridge.

3 On-site monitoring

The field test campaign was aimed at obtaining the strain distribution of the arch and its dynamic behavior subjected to dynamic moving loads via the application of the DFOS measurement technique. This section describes the application of DFOS sensing technology in monitoring the investigated span of the masonry arch rail bridge, including details about the instrumentation, the operational conditions during measurements, and the testing procedures.

3.1 Instrumentation

The ODiSI-B series integrator is a distributed fiber optic analyzer, based on the Rayleigh scattering, designed by American company Luna Innovations and specifically engineered to embrace the testing challenges of advanced materials and systems. This system has been used for the present bridge application. It provides high-speed, fully distributed strain, and temperature measurements with high spatial resolution, with hundreds of sensing locations per meter on a single fiber, all of them being interrogated simultaneously at frequencies up to 250 Hz. In contrast to conventional sensors (such as strain gages and FBG sensors), the system measures strain data using the swept-wavelength coherent interferometry technique, with a standard fiber serving as the sensing element. Each point along the fiber can be considered a

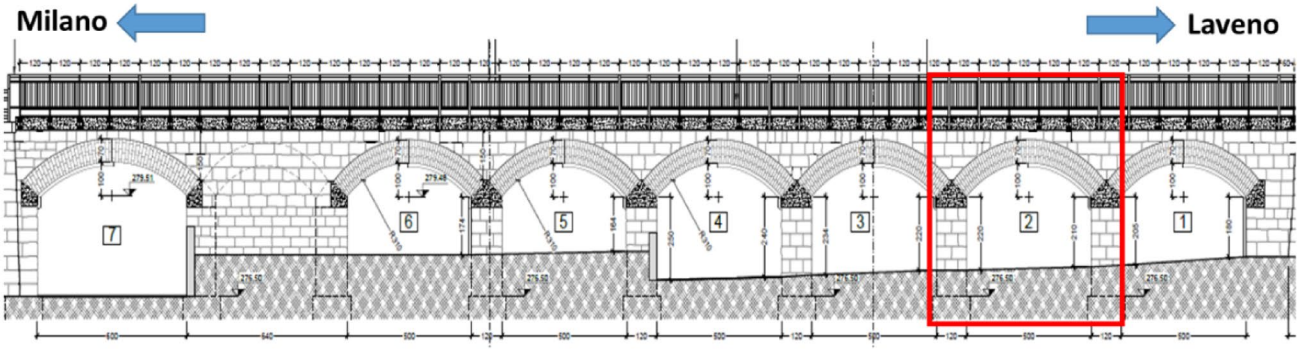

(a) South-West view

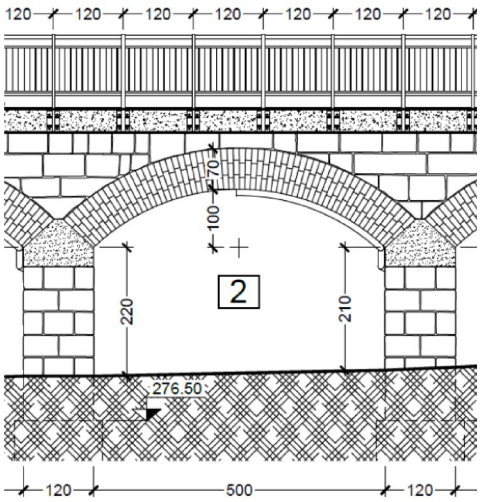

(b) Side view

Fig. 1 The views of the investigated span (Span 2) of the bridge

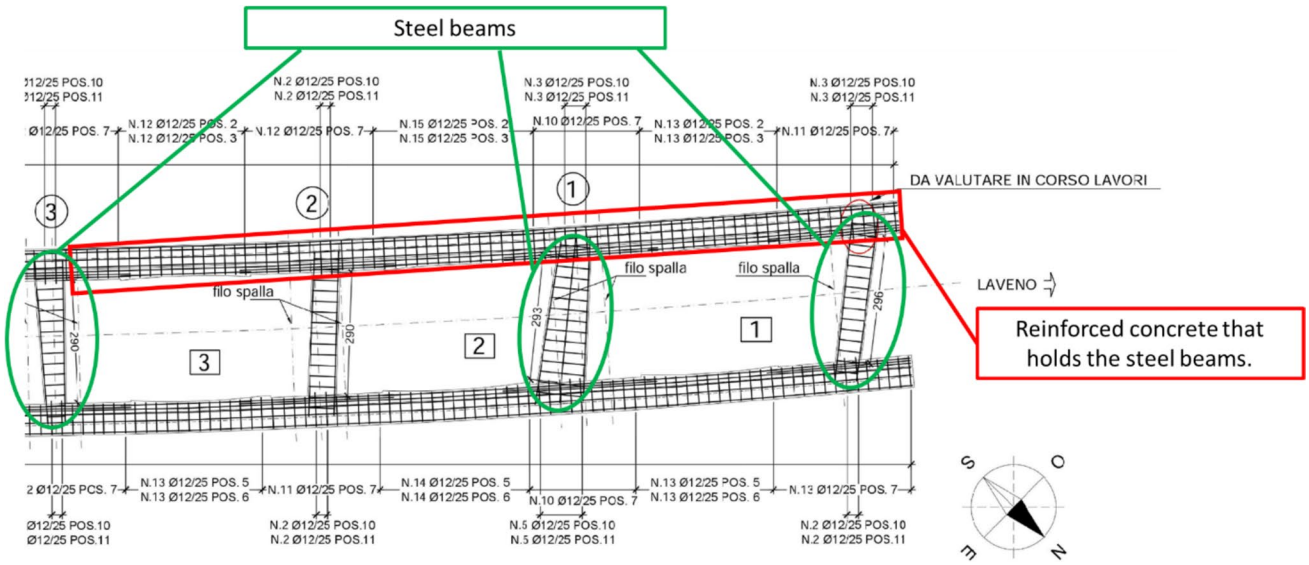

Fig. 2 Top view of the bridge

sensor, capable of monitoring strain and temperature values, with a high spatial resolution.

As illustrated in Fig. 3, the measuring signal received from the fiber is segmented into numerous small windows. The signals from each section are converted to their respective frequency ranges. And any local changes leading to spatial stretches or compressions of the local reflective index along the glass fiber are manifested as a frequency shift Δf in the spectrum of light scattered in the fiber. As a consequence, these changes can be converted into changes in local temperature or strain values.

Such spectral shift in response to strain ε or temperature T is analogous to the change in resonant wavelength $\Delta\lambda$ or spectral shift $\Delta\nu$ of a Bragg grating, as indicated in Eq. (1).

$$\frac{\Delta\lambda}{\lambda} = \frac{\Delta\nu}{\nu} = K_T T + K_\varepsilon \varepsilon \tag{1}$$

where λ and ν denote the mean optical wavelength and frequency, and K_T and K_ε are the temperature and strain calibration constants with default values of $6.45 \times 10^{-6}\,K^{-1}$ and 0.780, respectively.

In this experimental campaign, Luna's high-definition (HD) strain sensor, known for its low-profile and flexibility, has been selected as the preferred solution for monitoring dynamic strains in a masonry bridge through the ODiSI measurement system. This sensor is capable of achieving ultra-high resolution strain measurements, even when dealing with gage pitches as fine as 0.65 mm. The sensing fibers are polyimide coated low bend loss fiber include a diameter of 155 µm, an operational range spanning from − 40 to 300 °C, and compatibility with LC/APC connectors.

The system is capable of performing static and dynamic measurements over sensing distances of up to 20 m and sampling rates of up to 250 Hz. Notably, this study considers only a 2.15 m sensing area with a spatial resolution of 2.56 mm in the investigated span as a preliminary attempt

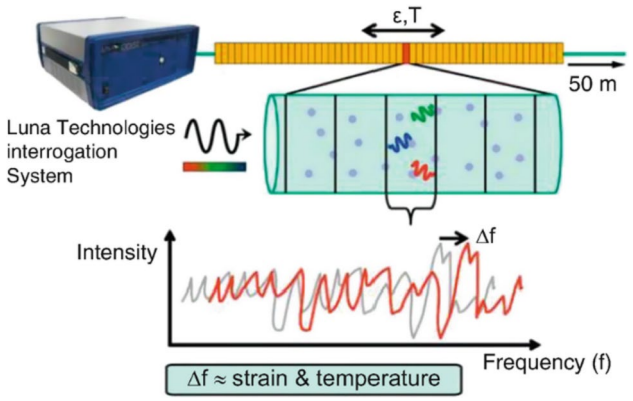

Fig. 3 Effect of strain or temperature on measured frequency responses [24]

(Span 2, Fig. 1b). This was also owing to an original failure in which we applied a 20-m fiber but the fiber was damaged during the gluing process due to the vulnerability of the bare fiber.

Figure 6 shows the entire test scene, in which the fiber optic, denoted by the red curve, was bonded to the center of the arch, from the top of the left abutment to about 1/3 of the left side of the arch barrel (Fig. 4).

The most frequently observed pattern of failure in masonry arch bridges is the formation of mechanisms. The formation of plastic hinges in the arch barrel is caused by the cracking of voussoirs, mortar joints, or bond failure between the two [25]. The hinges can be formed beneath the loads at or near the abutment and in close proximity to the opposite quarter span. Recent years have seen an increase in the interest for research into the possible failure mechanisms, particularly when determining the ultimate strength of bridges. From theoretical models to advanced numerical models to practical evaluation methods, a quantum leap has been made. However, these methods are beyond the scope of this paper and the interested readers may find more details in references in [26–30]. The observation of a visible crack near the junction of the abutment and the arch at its next arch on the right (See Fig. 5) implies the risky impact from the hinges, often resulting in thin cracks. The investigated area, as illustrated in Fig. 4, covers the risky region of hinges that bear the highest stress.

While the added value of DFOS fiber sensors in monitoring a bridge's in-service behavior is unquestionable, a proper installation on the arch surface remains a challenge that requires additional effort. The applied fiber sensor is almost entirely exposed without a protection layer, preferably attached to a relatively smooth metallic or composite surface.

Due to the abrasive nature of the arch surface in the investigated area, we planned and followed the following routes in accordance with LUNA® official guidelines [31]. In general, it consists of three major steps: (1) Layout of the fiber route; (2) Surface preparation; and (3) Fiber bonding. Even if solutions exist for fibers embedded into a composite or fiberglass matrix, in this case, due to the complex surface status and the need to achieve the best adhesion of the fiber to the rough bridge surface, it was decided to work with the bare fiber.

Our planned measurement area focuses on the spatial continuous strain profile along the longitudinal midline of the arch up to 2.15 m, as indicated in Fig. 4. A few centimeters between the fiber optic sensor connectors will remain unbonded for calibration reasons and to maintain measurement quality and performance, removing the detrimental effects of a moving or vibrating standoff from the optical data before computing strain or temperature.

It is essential to have a chemically clean surface with the proper roughness for the adhesive to ensure the efficiency of

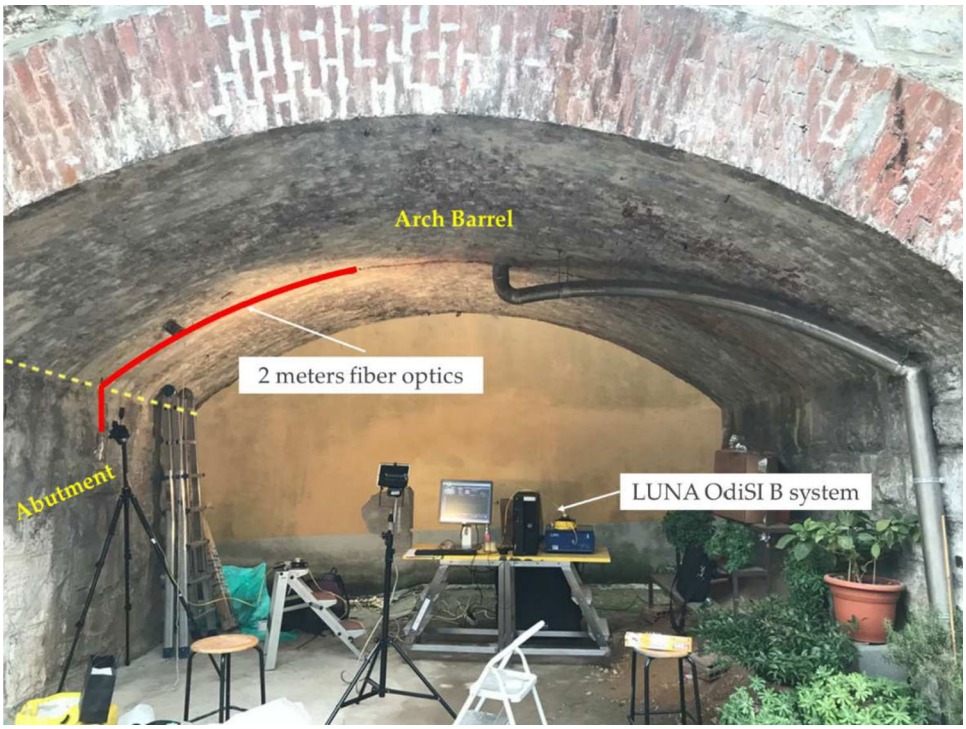

Fig. 4 Full view of the test

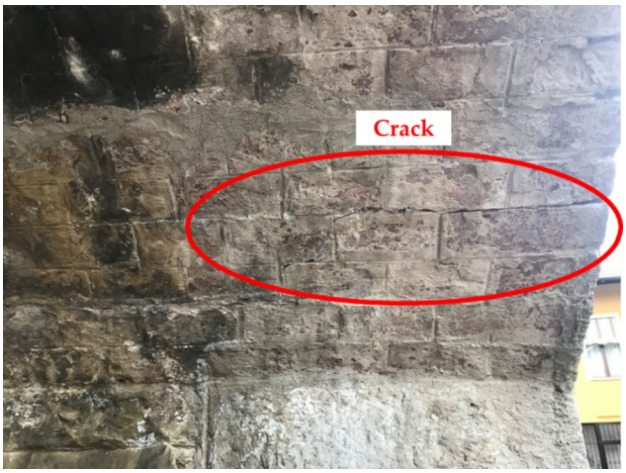

Fig. 5 The observable crack at the next arch

Fig. 6 The comparison between before and after polishing

strain transfer in the survey area. We began by rough sanding the intended area's surface with a polishing machine, followed by further smoothing the surface with abrasive paper. The comparison between before and after polishing is shown in Fig. 6. The final step is to apply the adhesive to the fiber and bond it to the polished area. The adhesive, a DP110 scotch-weld from 3 M®, used to bond the fiber, is a flexible and two-component epoxy adhesive, particularly designated for strong, permanent bond even under vibrations and impacts. Certainly bonding efficiency of the used adhesive is a concern, but potential data trends due to temperature changes can be disregarded because every transit takes such a short amount of time that the temperature can be held constant. Figure 7 displays the process of pasting the fiber and the state afterward, respectively.

3.2 Monitoring conditions

The monitoring campaign was carried out when commuter electric trains passed over the bridge. The trains are known

Fig. 7 The distributed fiber before and after gluing

as TAF (Treni Alta Frequentazione), designed by AnsaldoBreda and Firema Trasporti for high-density services, and have been in use since the late 1990s. These fixed-route trains have four carriages, have a good acceleration with a maximum speed of 140 km/h, and weigh about 210 tons.

4 Monitoring results

4.1 Data collection

The monitoring campaign has been carried out using the LUNA ODiSiB system, which consists of a distributed fiber optic system measuring data in the monitoring area and the associated analyzer. Due to the contact forces between the wheels and the track, the monitored bridge has a dynamic response when the train passes over the monitored bridge. The raw dynamic response data are then post-processed and analyzed to determine the health status of the monitored region.

Unlike conventional sensing techniques, which record strains only at discrete points, the DOFS measurement system enables access to a total number of 827 sensing points within the 2-m investigated region on the lower wall of the arch (as shown in Fig. 4). Thus, the DOFS measurements can be used to generate a quasi-full-field strain distribution under traffic loads, which can aid in visualizing the strain distribution from an engineering standpoint.

As an example, Fig. 8 displays the time domain plot of the strain detected at each sensing point during the pass-by of one Laveno–Milano train at around 12:52 on 14/11/2019.The entire measurement process continued for 20 s with a sampling frequency of 250 Hz. From the depicted time domain plots, some positive/negative fluctuations or peaks can be noticed.

Since conventional discrete FBG sensors can only gather temporal information at a few specific locations, in many cases, these sensors cannot fully describe the phenomenon at a specific and well-defined location and at a specific time, making it hard to achieve a high resolution in time and space at the same time. Benefiting from the advantage of having both temporal and spatial sensing data continuously with DOFS, a better visual description in the time–space domain is possible. Figure 9 shows a 3D view of the strain profile across both time and dense sensor locations.

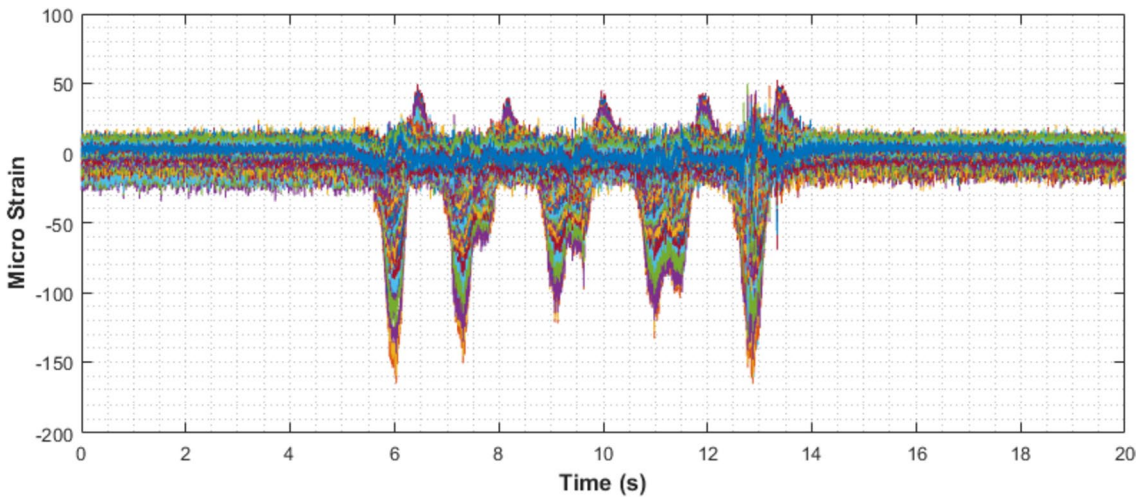

Fig. 8 The measured strains by the entire DOFS sensors in the time domain

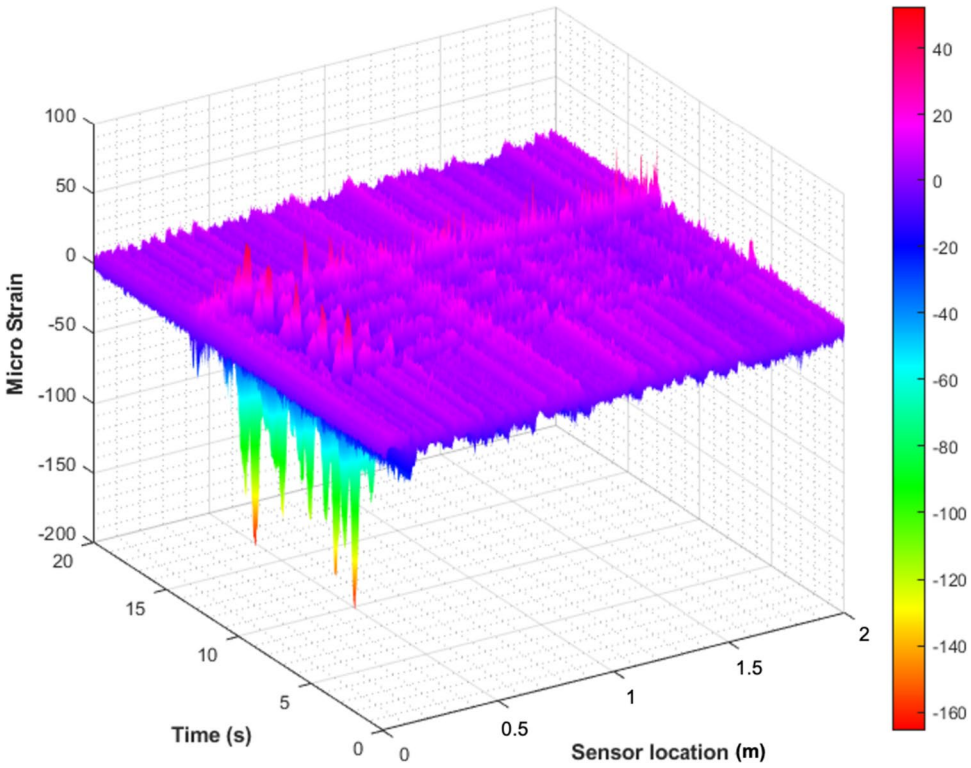

Fig. 9 The measured strains by the entire DOFS sensors in the time–space domain

4.2 Data analysis

Figure 10 presents the strain detected by the distributed fiber around the abutment–arch joint of Span 2, measured by the fiber optic sensor No. 100. The positive and negative strain values represent tensile and compression strains, respectively. The eight negative peaks in Fig. 10 point out the eight individual bogie passages (wheel–track

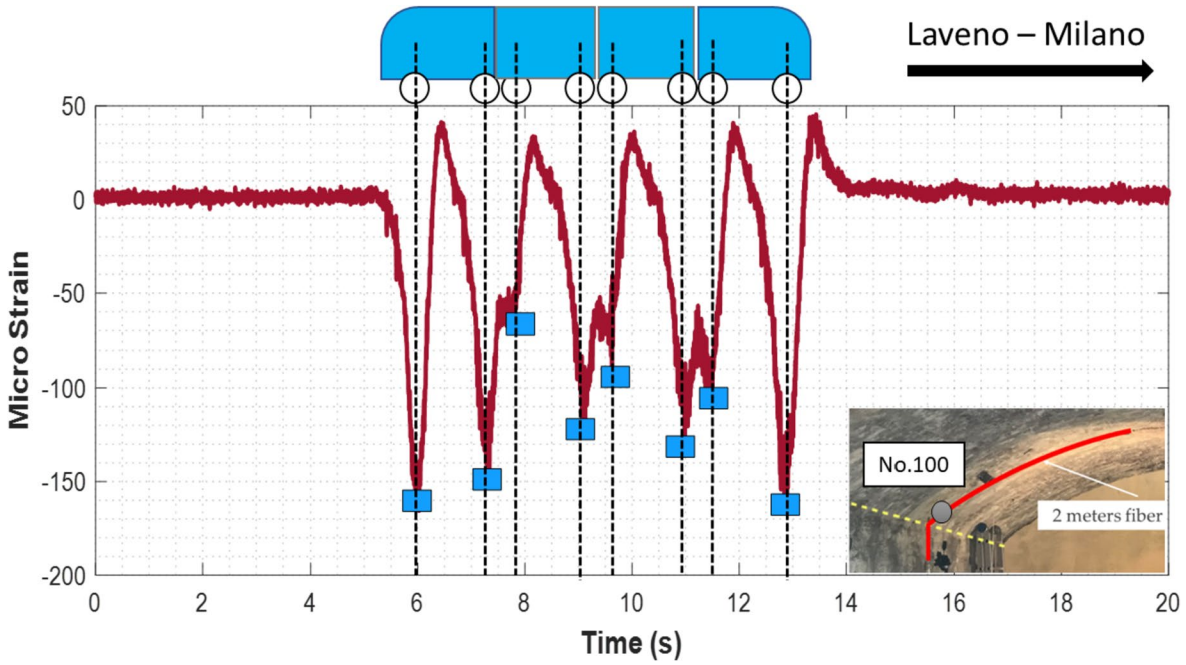

Fig. 10 The measured strains by DOFS sensor No. 100 in the time domain

contact behavior). As trains pass over any given location, they cause movement of the track surface. This is mainly due to the bending of the track, the compression of the ballast, and the voids under the sleepers (see for example [32]). Therefore, from a health assessment perspective, understanding the level of impact on the masonry arch rail bridge caused by traffic loads is of primary concern.

It is also worth noting that the locomotives and car bodies can be easily identified by looking at the strain data in Fig. 10. The first and last negative peaks on the left and right are the bogies of the locomotive producing a value of around − 165.6 με. And the peaks in between reflect the bogies of the car bodies, which have mass lower than locomotives. In Figs. 8, 9, 10, the positive strain peaks indicate that peaks do not always return to the unloaded level. This is because there is an immediate elastic recovery, followed by a long and very slow return back to the initial position.

In contrast to a point sensor, which produces the relative maximum peak at a single location, the ability to simultaneously measure strain at all nearby locations produces the absolute maximum peak, allowing for the detection of the most critical position.

The eight negative peaks in Fig. 10 occur at 6.03/7.31/7.79/9.13/9.63/10.99/11.48/12.88 s, respectively. Figure 11 demonstrates the strain distribution across the fibers at the eight-time instants. Apart from the discrepancy in amplitude, the trend of the strains in the observation region remains consistent. This can be due to the presence of the whole train or only a portion of it on the measurement position.

Figure 12a–f illustrates the time domain strains acquired during the transit of six subsequent pass-by trains. It's worth noting that the variation in the peak-to-peak time lags for each load case is actually due to the trains' different speeds. The train was decelerating in the Milano–Laveno direction while accelerating on the Laveno–Milano route.

To further illustrate the strain profile created by the moving load of the train in motion, the strains at the sensors corresponding to the eight peaks across the entire fiber for each load case have been summarized in Fig. 13a–f. Strains across the entire investigated region exhibit a similar pattern for each load case, with the largest negative strain values ranging between − 160 and − 170 με. And, in the majority of cases, peak 1 and peak 8 caused by the combined loads of both locomotives are dominant in comparison to other peak values.

Table 1 summarizes the strains before/during/after training passing measured from sensor 100. More specifically, it lists the mean ± STD strain status before and after training passing (pre-and post-loading), as well as the maximum negative strains experienced during train loading. Trains were nearly empty, and the presence of passengers does not significantly alter the total mass. If we consider the pulled car as an example, its mass of 44t 100 pax at an average of 80 kg results in an added mass of 18% of the original; when we consider the locomotive, this value drops to 12%. Therefore, it can be seen that the maximum strain under moving load fluctuates within a narrow range, whereas the unloading strain before and after the train passes falls in a very small range, literally demonstrating the robustness of the measurement system.

4.3 Frequency analysis

With further investigation of the collected data, another striking observation is that the maximum negative distinct peak always occurs at a distance of approximately 0.2586 m from the left abutment (Fig. 4) according to Fig. 11 and

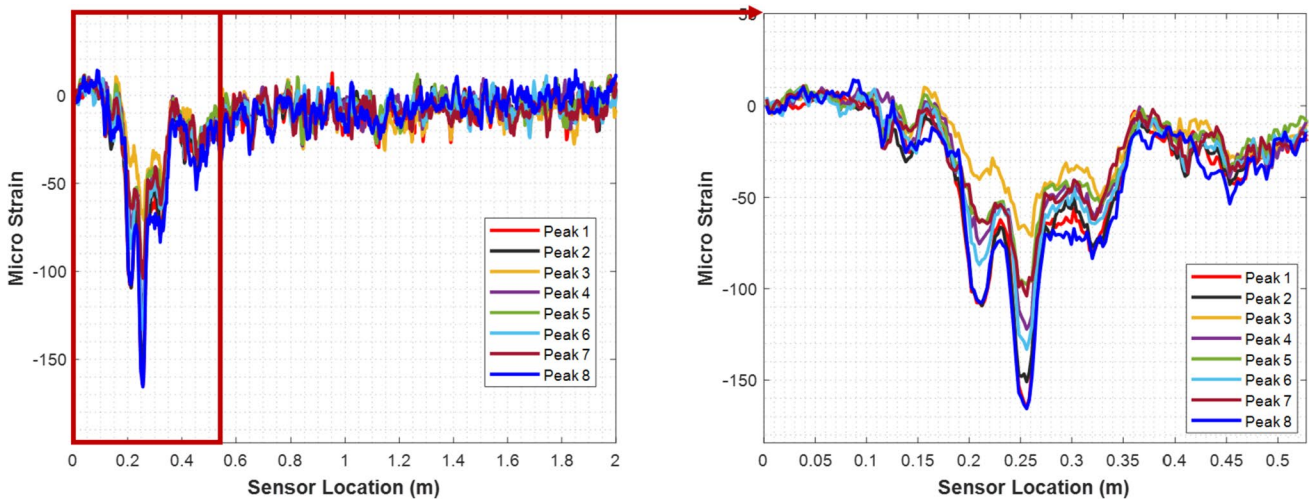

Fig. 11 The strains at the sensors corresponding to the eight peaks across the entire fiber

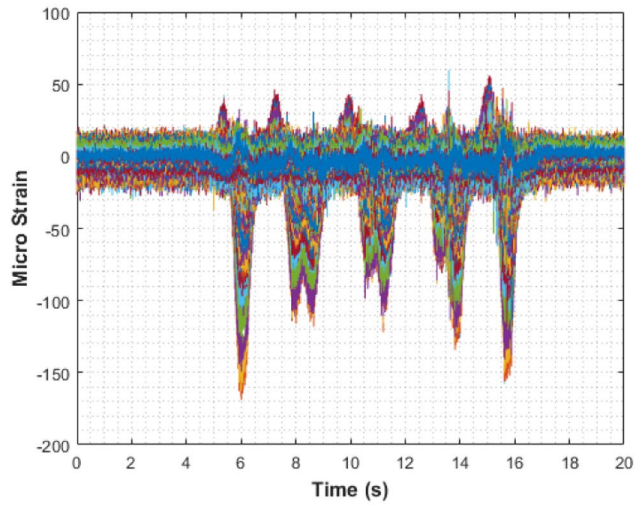

(a) Milano-Laveno 13:06

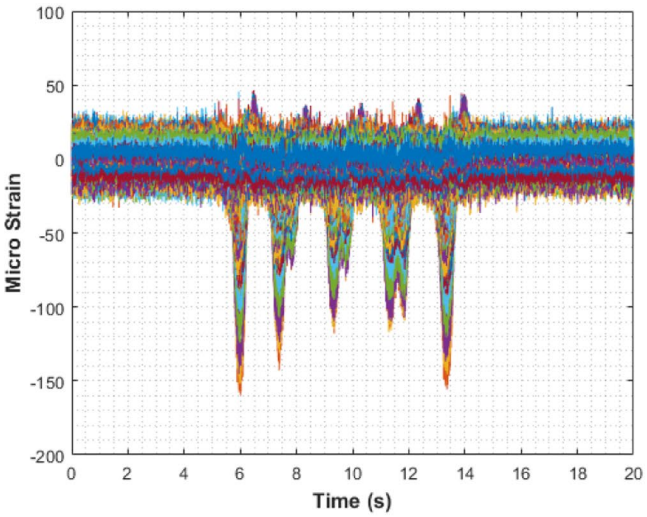

(b) Laveno-Milano 13:22

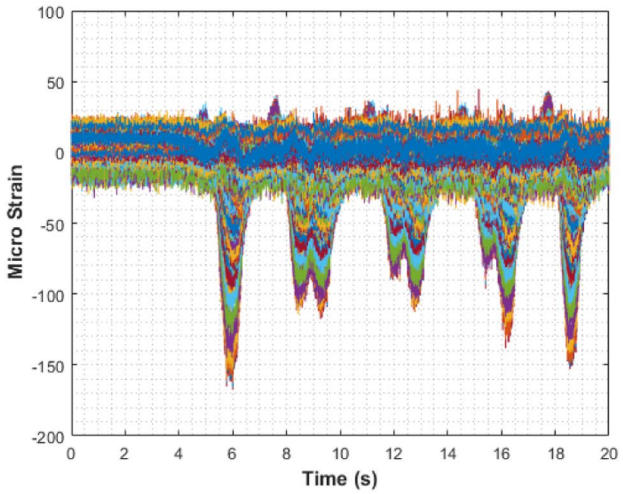

(c) Milano-Laveno 13:36

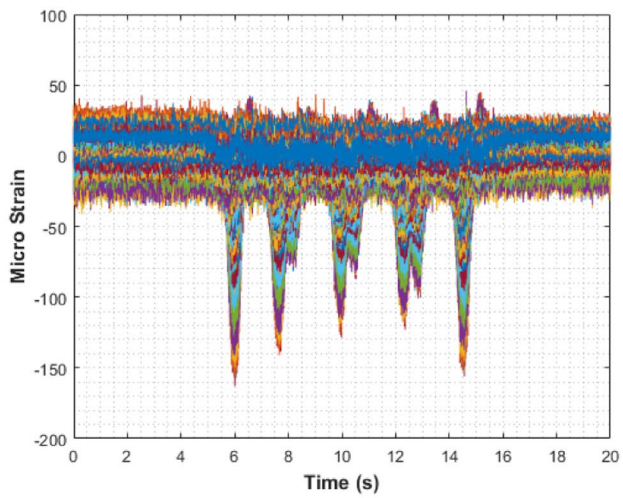

(d) Laveno-Milano 13:52

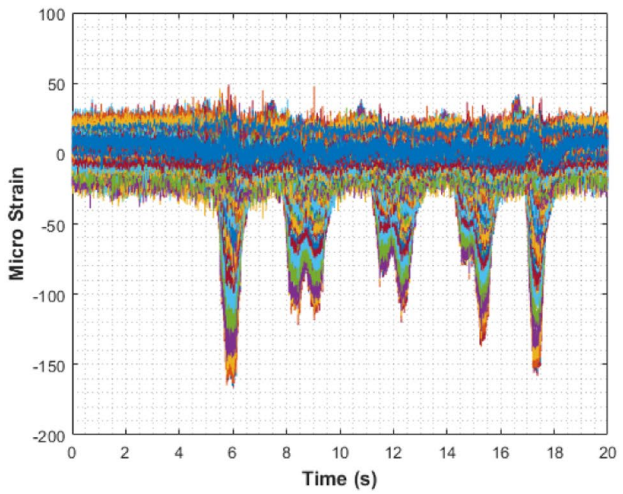

(e) Milano-Laveno 14:06

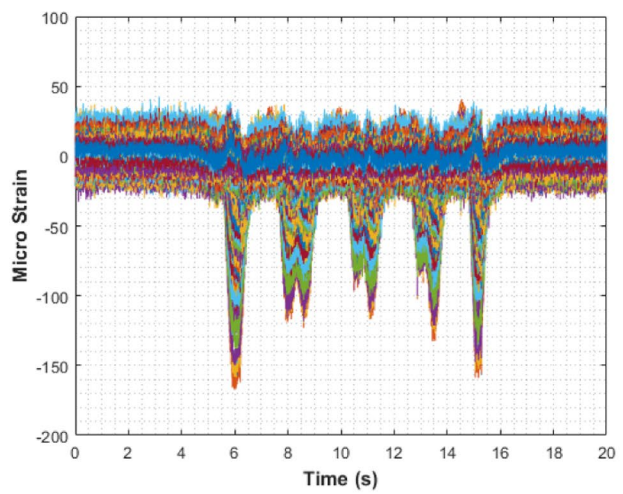

(f) Milano-Laveno 15:06

Fig. 12 The measured strains by the entire DOFS sensors in the time domain when six different trains passed over the bridge

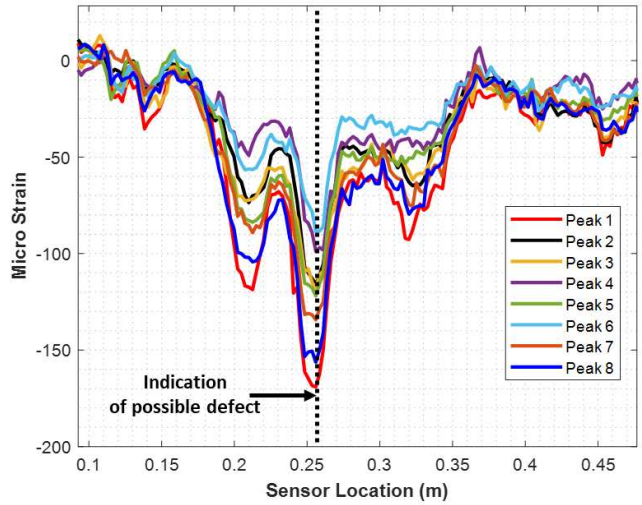

(a) Milano-Laveno 13:06

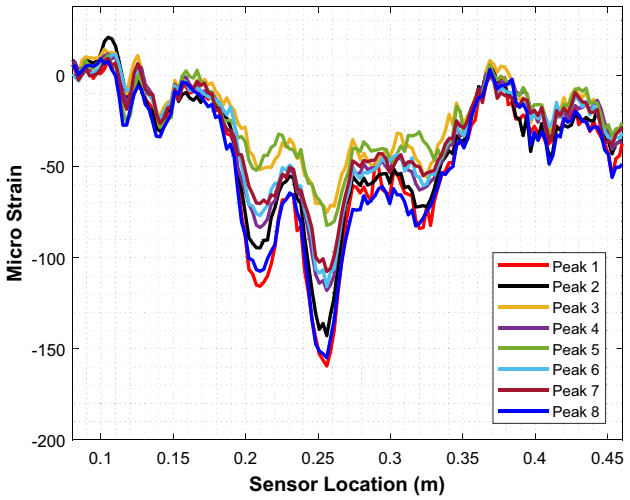

(b) Laveno-Milano 13:22

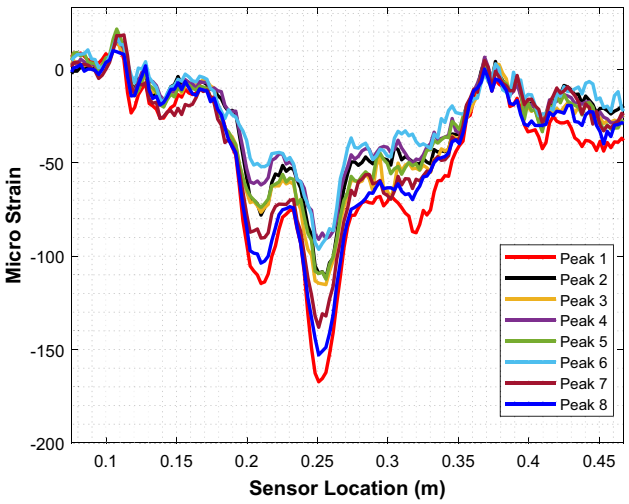

(c) Milano-Laveno 13:36

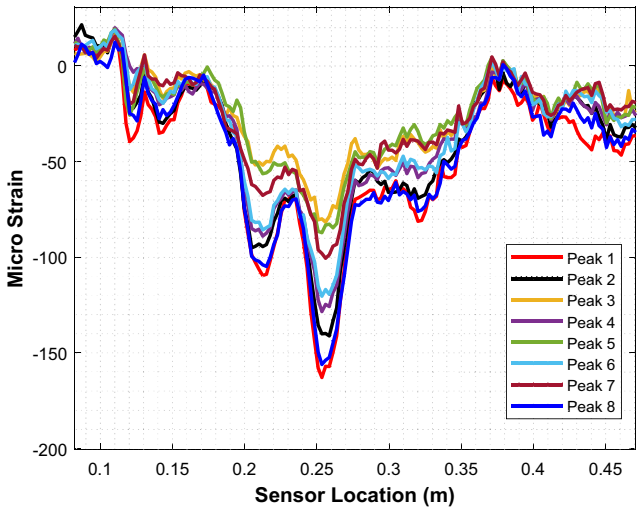

(d) Laveno-Milano 13:52

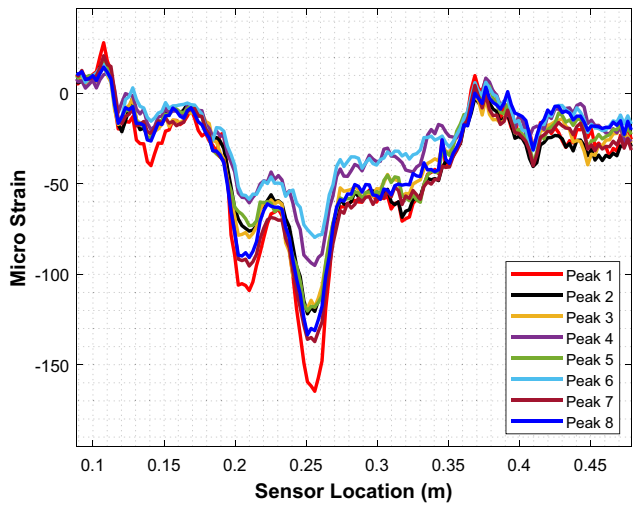

(e) Milano-Laveno 14:06

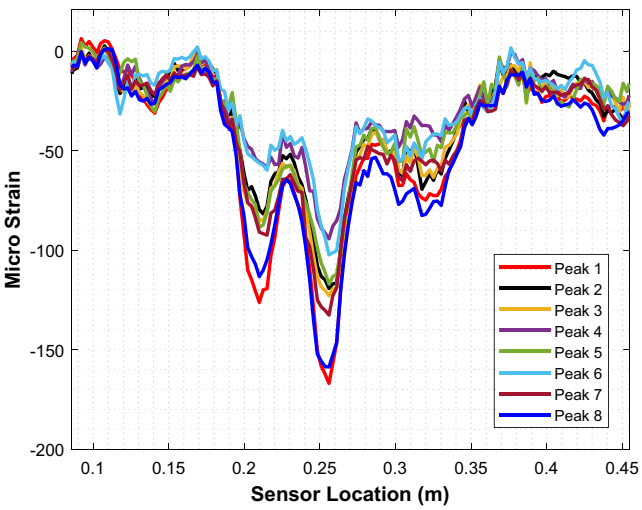

(f) Milano-Laveno 15:06

Fig. 13 The strains at the sensors corresponding to the eight peaks across the entire fiber at different moments

Table 1 The strains before/during/after train passing measured from sensor 100

	Before training passing (mean ± STD strain με)	During train passing (maximum strain με)	After train passing (mean ± STD strain με)
Laveno–Milano 12:52	1.21 ± 1.65	− 165.6	2.76 ± 1.69
Milano–Laveno 13:06	0.68 ± 1.76	− 169.1	3.05 ± 1.72
Laveno–Milano 13:22	2.60 ± 2.13	− 159.5	3.96 ± 2.13
Milano–Laveno 13:36	1.90 ± 1.84	− 161.1	3.13 ± 1.91
Laveno–Milano 13:52	2.85 ± 0.02	− 157.0	2.96 ± 2.81
Milano–Laveno 14:06	2.89 ± 2.37	− 164.7	4.96 ± 2.01
Milano–Laveno 15:06	4.78 ± 2.08	− 166.7	5.64 ± 1.88

Fig. 13a–f. This information catches our attention because hinges bear the greatest amount of stress in the investigated region.

Figure 14 shows the power spectral density (PSD) [33] of the data from sensor No.100, along with a locally zoomed-in plot in dB/linear scale for the frequency range [0, 3 Hz]. From the PSD diagram, several dominant peaks can be visualized using a peak-picking estimation in the frequency domain. However, it is important to note that these values are not related to the masonry arch rail bridge's modal frequencies but rather to periodic loading due to the bogies' transit. For example, the peak-to-peak time in Fig. 12 is approximately 1.8 s, which is nearly identical to the frequency component of 0.58 Hz in Fig. 14. This is a prelude to stating that, even if we look for the presence of some dynamic behavior, its presence cannot be determined.

Additionally, it is worth noting the spectrogram of the data from sensor No. 100 in Fig. 15, which clearly indicates the number of locomotives/car bodies by virtue of the color intensity's high contrast.

In addition to the frequency analysis described above, additional investigations, such as damage detection and identification, may be conducted and implemented, as damage detection is critical for structural integrity. For example, the distinct peaks in Fig. 13a–f may relate purely to internal damage (e.g., cracks), hinge position, or a mixture of these. This, however, is beyond the scope of this work.

4.4 Further investigations

To further validate the measurement accuracy and assess the uncertainty of the distributed fiber solution, an investigation has been carried out about whether the train passing over the sensed area really resulted in the maximum strain, in the same position defined by the theoretical approaches. The following summarizes the primary implementation steps:

1. Compute the cross-correlation of each sensor with one of them serving as the reference, in order to determine the time delay Δt_i between the reference sensor and the generic ith sensor (we recall that in this case, we have a sensor spacing in the order of millimeters). Notably, the train speed can be roughly inferred based on the computed time delay and the distance between two sensors.

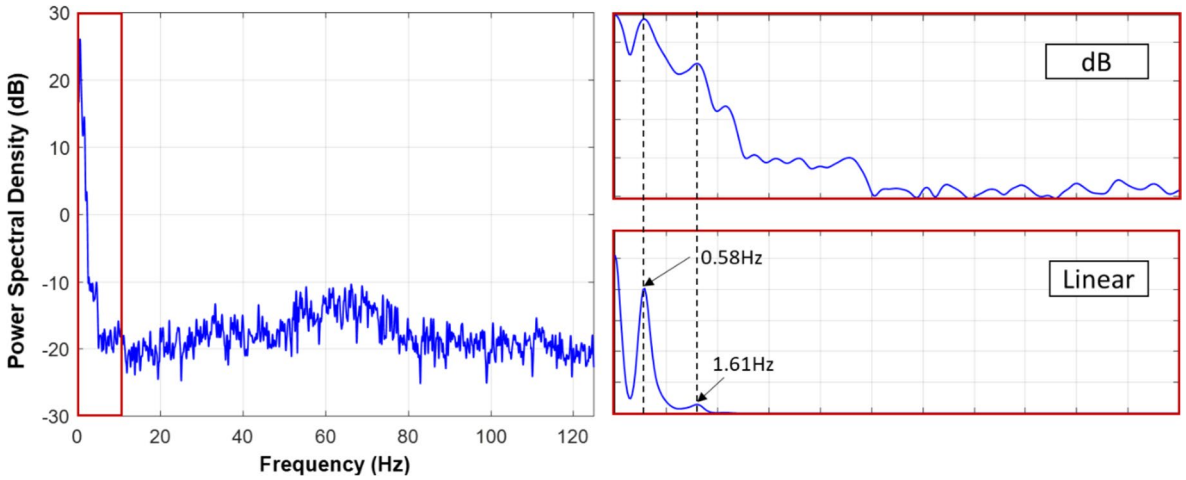

Fig. 14 PSD diagram of sensor No.100

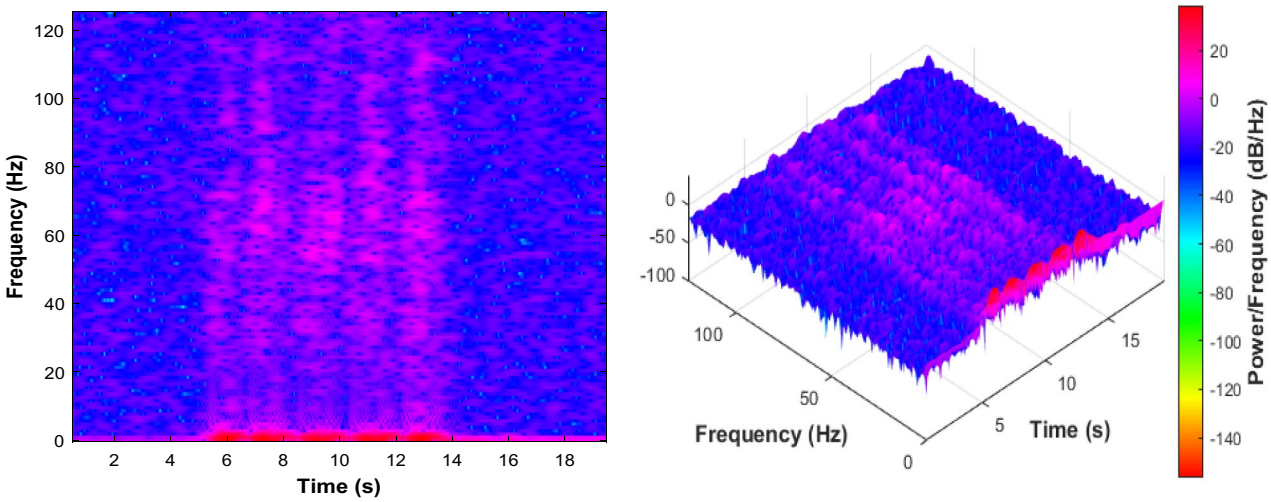

Fig. 15 Spectrogram diagram of sensor No. 100

2. Trace the strains over other sensors by first estimating the time t_M at which the referenced sensor measures the maximum strain (Fig. 16). Then we consider the strain S_i measured by the ith sensor at the time $t_M + \Delta t_i$ with the goal of confirming that the measured maximum strain closely matches the strain tendency shown in Fig. 13.
3. Compute the MS ratio, defined as the strain S_i obtained at any ith sensor over the maximum strain at the referenced sensor.

The following section details these three primary steps and discuss the meaning of the proposed MS ratio.

STEP 1: Time delay using cross-correlation analysis.

Correlation analyses are performed on all sensors after having chosen the reference sensor (sensor 80 in our case), with the mathematical expression (2) below

$$R_{x_i,x_{ref}}(k) = \frac{1}{N}\sum_{j=0}^{N-1} x_i(j)x_{ref}(j-k) \qquad (2)$$
$$i = ref, \quad ref+1, \ldots, 827$$

In Eq. (2), $R_{x_i,x_{ref}}(k)$ denotes the cross-correlation values between the reference sensor $x_{ref}(ref = 80)$ and all the other sensors $x_i(i = ref, ref + 1, ..., 827)$ and at a delay $t = \frac{f_s}{N}k$, in which f_s and N stand for the sampling frequency and the number of sampling points, respectively. As an illustration, in the following, we will refer to the strains measured during the train transit at 12:52. This will serve as a basis for discussion and the other cases have provided similar results.

Figure 16 illustrates the time histories of the reference sensor 80 and sensor 100 over the period [5 s, 15 s], revealing a similar strain trend though with different peak

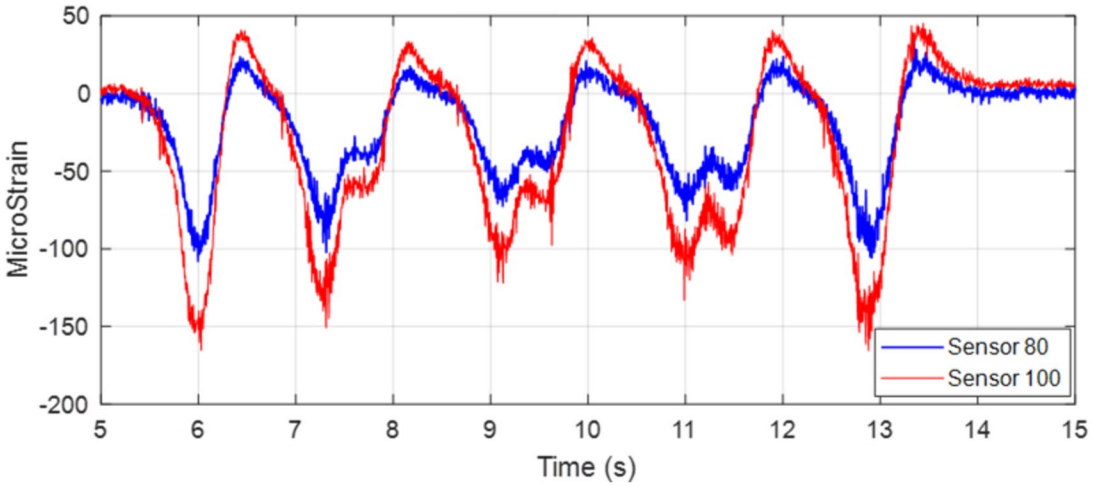

Fig. 16 Time histories of sensor 80 and sensor 100

amplitudes while a delay is not clearly identified from the time records.

The peak value in Fig. 17, providing the cross-correlation between the two sensors (sensors 80 and 100 during the train passage), corresponds to a delay of 8 ms. Delay over all the other sensors can be computed likewise and the summary is provided in Fig. 18.

The results of Fig. 18 show that the delay is approximately linearly related to the sensor location. The scattering occurring among measurements may be caused by measurement outliers and noise, which, in case of distributed sensing, still need proper assessment, especially in case of dynamic measurements.

Moreover, the train speed can be approximately determined using Eq. (3), once given the approximate computed delay and distance between sensors 80 and 100 or any other couple of close sensors.

$$V = distance(sensor80, sensor100)/\text{delay}(sensor80, sensor100) \quad (3)$$

As shown in Eq. (3), the distance between these two sensors is equal to the spatial resolution multiplied by the number of sensors in between, yielding a value of 48.64 mm. As a result, the train speed can be calculated as a reasonable value of 21.9 km/h, considering the train is slowing down or speeding up (the bridge is located only a few tens of meters from a station where all trains come to a halt).

STEP 2: Tracing the strains over other sensors.

Through the delay values derived from STEP 1, it is possible to ascertain whether the maximum strain is experienced at the same specific sensor location for all the bogies composing the train. This process is simply described in Eq. (4).

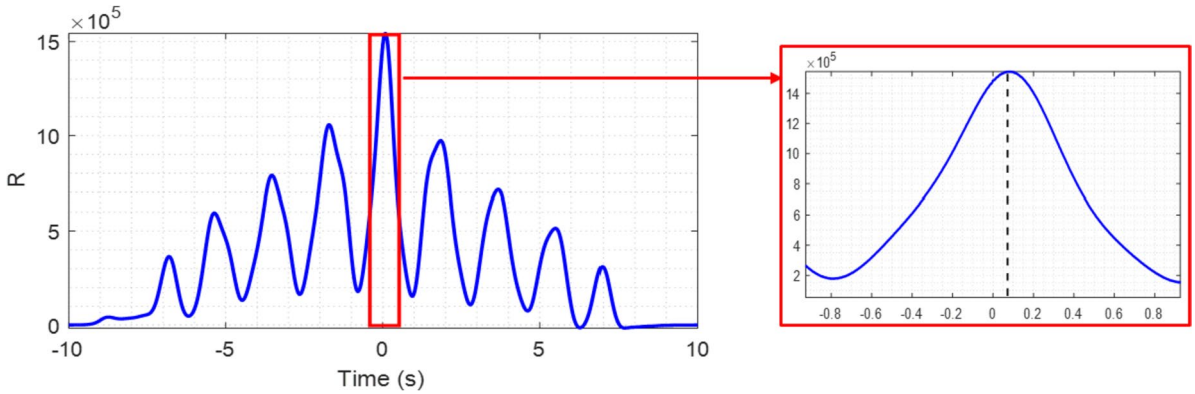

Fig. 17 Cross-correlation analysis between sensor 80 and sensor 100

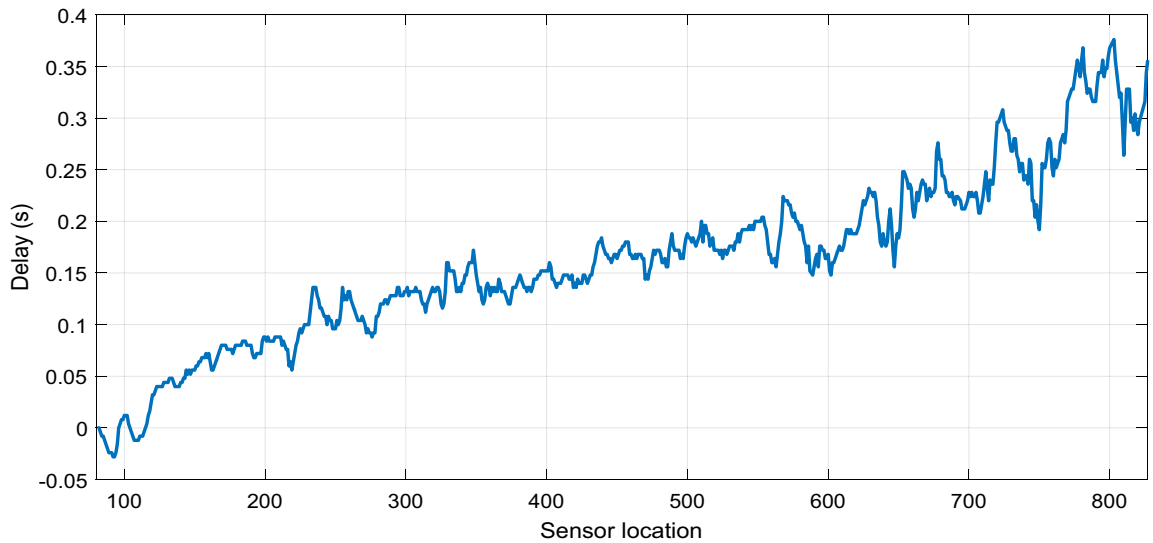

Fig. 18 Delay over all the other sensors

$$S(i) = Data_i(\text{delay}(sensor80, sensori)) \tag{4}$$

in which $Data_i(delay(sensor80, sensori))$ stands for the maximum strain measured by sensor i after the delay time between sensor 80 and sensor i.

STEP 3: MS Ratio calculation.

After normalization with the maximum strain at the reference sensor, the strains obtained in STEP 2 are termed as MS Ratio and given in Eq. (5): this is simply the ratio between the actual peak strain level and the reference sensor's maximum strain (Fig. 19).

$$MSRatio(i) = S(i)/\max(Data_{80}) \tag{5}$$

The maximum MS ratio is observed at sensor 100, which corresponds to the observation made in Sect. 4.3, subject to the maximum stress from train loading. Additionally, Fig. 20 summarizes the MS ratios for other train passes, in order to compare the trends in amplitude levels.

From Fig. 20, it is confirmed that MS ratios under the seven considered scenarios are nearly constant in terms of the amplitude level, albeit with a slight oscillation which can find an easy explanation in the different wheel status, the different loads, the different stiffness. The highest MS ratios are almost always found at the same sensor (sensor 100, meaning) the same position. These findings can help to increase confidence in the dynamic measurements performed with distributed fiber optics, which offers a deeper insight into a series of problems hardly addressed by the use of more common vibration sensors.

5 Conclusions

In this study, monitoring the dynamic behaviors of a masonry arch rail bridge in Italy using distributed fiber optic sensor DFOS is preliminarily investigated. The fundamental aim of this research work was to perform on-site monitoring and study the feasibility of the use of DFOS to reveal the dynamic behaviors of masonry arch rail bridges. With the Luna ODiSI-B® system, some preliminary results have been presented, demonstrating promising measurements and

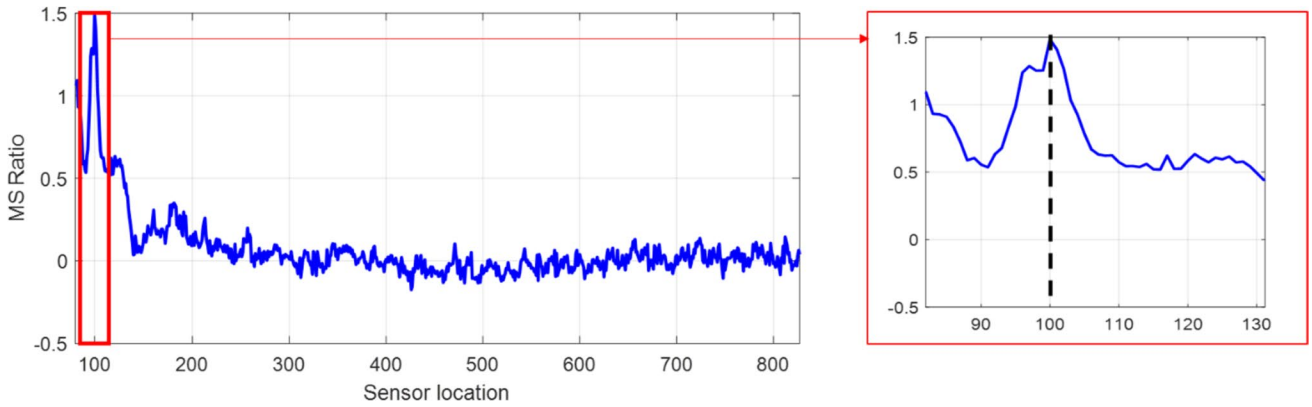

Fig. 19 MS Ratio from sensor 89 to sensor 827

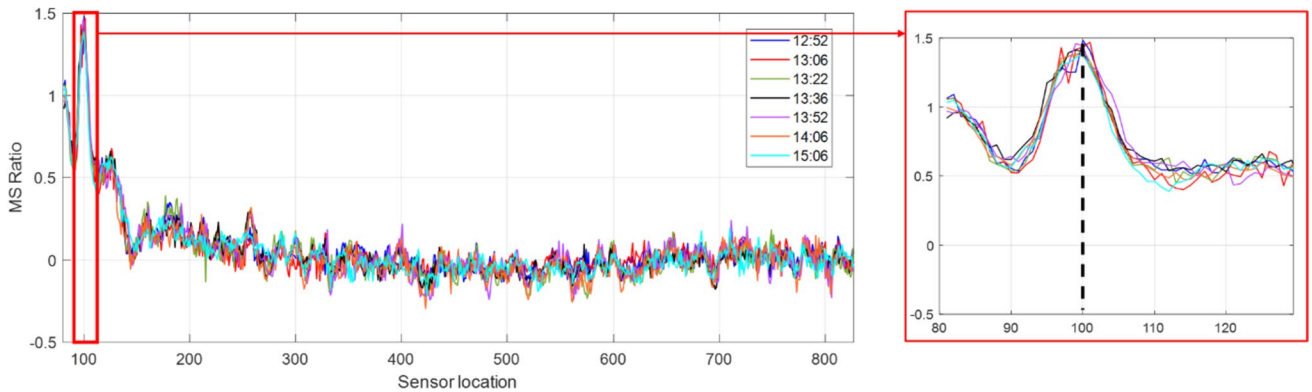

Fig. 20 MS ratios of the measured strains at seven different train passing moments

interesting results enriching the information about the conditions of a masonry arch bridge.

The number of locomotives and car bodies can be clearly identified by analyzing the dynamic response in the time domain from the fiber sensors attached to the inner surface of the investigated arch. This is independent from the train direction and its speed.

Thanks to the dense solution provided by DFOS technique, any anomaly can be detected with a good localization in space. Specifically, a strain peak was identified around the joint between the arch in Span 2 and the abutment in the region of interest, which could be due to internal damage (e.g., cracks), hinge position, or a combination of these. This explanation can be confirmed in both the available literature on arch bridges and by the presence of a visible crack at roughly the same location in the adjacent arch.

The authors anticipate that the knowledge and the experience gained through this study will aid in developing guidelines for new masonry railroad bridge monitoring campaigns, particularly when combined with DFOS measurement techniques. Additionally, for further investigations, the use of long fibers covering a larger sensing area under a variety of operating conditions, including ambient vibration, will be investigated, as well as the use of more advanced signal processing and damage detection techniques.

Acknowledgements The authors would like to acknowledge that this work was supported by the UK Engineering and Physical Science Research Council via a knowledge transfer account (KTA) to The University of Sheffield, UK. Moreover, the authors would like to acknowledge the company Ferrovie Nord S.p.A. for the availability of the tested bridge as well as for the support to the development of the tests.

References

1. Orbán Z (2007) UIC project on assessment, inspection and maintenance of masonry arch railway bridges. ARCH 7:3–12
2. Küttenbaum S, Maack S, Taffe A (2018) Structural safety referring to ultrasound on concrete bridges: from non-valuated measurands to reliable knowledge about the inner construction without destructive interventions. Beton-und Stahlbetonbau 113:7–13
3. Wilkinson S, Duke SM (2014) Comparative testing of radiographic testing, ultrasonic testing and phased array advanced ultrasonic testing non destructive testing techniques in accordance with the AWS D1. 5 bridge welding code (No. BDK84-977-26). Florida. Dept. of Transportation
4. Nassif HH, Gindy M, Davis J (2005) Comparison of laser Doppler vibrometer with contact sensors for monitoring bridge deflection and vibration. NDT E Int 38(3):213–218
5. Zhao X, Liu H, Yu Y, Xu X, Hu W, Li M, Ou J (2015) Bridge displacement monitoring method based on laser projection-sensing technology. Sensors 15(4):8444–8463
6. Colla C, Das PC, McCann D, Forde MC (1997) Sonic, electromagnetic and impulse radar investigation of stone masonry bridges. NDT E Int 30(4):249–254
7. Pieraccini M, Miccinesi L (2019) An interferometric MIMO radar for bridge monitoring. IEEE Geosci Remote Sens Lett 16(9):1383–1387
8. Bhure H, Sidh G, Gharad A (2018) Dynamic analysis of metro rail bridge subjected to moving loads considering soil–structure interaction. Int J Adv Struct Eng 10(3):285–294
9. Meng X, Dodson AH, Roberts GW (2007) Detecting bridge dynamics with GPS and triaxial accelerometers. Eng Struct 29(11):3178–3184
10. Sung SH, Park JW, Nagayama T, Jung HJ (2013) A multi-scale sensing and diagnosis system combining accelerometers and gyroscopes for bridge health monitoring. Smart Mater Struct 23(1):015005
11. Hoag A, Hoult NA, Take WA, Moreu F, Le H, Tolikonda V (2017) Measuring displacements of a railroad bridge using DIC and accelerometers. Smart Struct Syst 19(2):225–236
12. Murray C, Hoag A, Hoult NA, Take WA (2015) Field monitoring of a bridge using digital image correlation. Proc Inst Civ Eng-Bridge Eng 168(1):3–12
13. Koltsida I, Tomor A, Booth C (2013) The use of digital image correlation technique for monitoring masonry arch bridges
14. Li C, Sun L, Xu Z, Wu X, Liang T, Shi W (2020) Experimental investigation and error analysis of high precision FBG displacement sensor for structural health monitoring. Int J Struct Stab Dyn 20(06):2040011
15. Lim KS, Zaini MKA, Ong ZC, Abas FZM, Salim MABM, Ahmad H (2020) Vibration mode analysis for a suspension bridge by using low-frequency cantilever-based FBG accelerometer array. IEEE Trans Instrum Meas 70:1–8
16. Cocking S, Alexakis H, DeJong M (2021) Distributed dynamic fibre-optic strain monitoring of the behaviour of a skewed masonry arch railway bridge. J Civ Struct Health Monit 11:1–24
17. Yu Y, Vergori E, Worwood D, Tripathy Y, Guo Y, Somá A, Marco J (2021) Distributed thermal monitoring of lithium ion batteries with optical fibre sensors. J Energy Storage 39:102560
18. Saidi M, Gabor A (2020) Experimental analysis of the tensile behaviour of textile reinforced cementitious matrix composites using distributed fibre optic sensing (DFOS) technology. Constr Build Mater 230:117027
19. Bao X, Chen L (2012) Recent progress in distributed fiber optic sensors. Sensors 12(7):8601–8639
20. Cheng L, Cigada A (2017) Experimental strain modal analysis for beam-like structure by using distributed fiber optics and its damage detection. Meas Sci Technol 28(7):074001
21. Cheng L, Cigada A, Lang ZQ, Zappa E (2019) Calibrating static measurement data from distributed fiber optics by the integration of limited FBG sensors based on the extended kernel regression method. Meas Sci Technol 30(12):125102
22. Cheng L, Cigada A, Lang Z, Zappa E, Zhu Y (2021) An output-only ARX model-based sensor fusion framework on structural dynamic measurements using distributed optical fiber sensors and fiber Bragg grating sensors. Mech Syst Signal Process 152:107439
23. LUNA Technologies (2017) ODiSI-B optical distributed sensor interrogator: User's guide

24. Samiec D (2012) Distributed fibre-optic temperature and strain measurement with extremely high spatial resolution in optical metrology. Polytec GmbH
25. Ford TE, Augarde CE, Tuxford SS (2003) Modelling masonry arch bridges using commercial finite element software. In: The 9th International Conference on Civil and Structural Engineering Computing, The Netherlands, pp 161–203
26. Ahmad SHS (2017) Static analysis of masonry arches. PhD thesis, University of Salford
27. Wang J, Melbourne C (2010) Mechanics of MEXE method for masonry arch bridge assessment. Proc Inst Civ Eng-Eng Comput Mech 163(3):187–202
28. Hughes TG, Blackler MJ, MEXE (1997) A review of the UK masonry arch assessment methods. Proc Inst Civ Eng-Struct Build 122(3):305–315
29. Gilbert M (2007) Limit analysis applied to masonry arch bridges: state-of-the-art and recent developments. In: 5th International arch bridges conference, pp 13–28
30. Gilbert M, Casapulla C, Ahmed HM (2006) Limit analysis of masonry block structures with non-associative frictional joints using linear programming. Comput Struct 84(13–14):873–887
31. ODiSI Fiber Optic Sensor Installation Guide. https://lunainc.com/sites/default/files/assets/files/resource-library/TN_Applying-Strain-Sensors_FINAL.pdf
32. Azizi M, Shahravi M, Ali ZJ (2021) Determination of wheel loading reduction in railway track with unsupported sleepers and rail irregularities. Proc Inst Mech Eng, Part F: J Rail Rapid Transit 235(5):631–643
33. Welch PD (1967) The use of fast fourier transform for the estimation of power spectra: a method based on time averaging over short, modified periodograms. IEEE Trans Audio Electroacoust 15:70–73